


 Cite this: *RSC Adv.*, 2023, **13**, 12663

Visible light driven reform of wasted plastics to generate green hydrogen over mesoporous ZnIn₂S₄†

 Yeqin Zheng,^{‡a} Ping Fan,^{‡b} Rongjie Guo,^b Xiaohui Liu,^a Xiantai Zhou,^{ID a} Can Xue^{ID *a} and Hongbing Ji^{ID *b}

As the global consumption of plastics keeps increasing, the accumulated plastics in the natural environment have threatened the survival of human beings. Photoreforming, as a simple and low-energy way, could transform wasted plastic into fuel and small organic chemicals at ambient temperature. However, the previously reported photocatalysts have some drawbacks, such as low efficiency, containing precious or toxic metal. Herein, a noble-free, non-toxic, and easy prepared mesoporous ZnIn₂S₄ photocatalyst has been applied in photoreforming of polylactic acid (PLA), polyethylene terephthalate (PET) and polyurethane (PU), generating small organic chemicals and H₂ fuel under simulated sunlight. Plastic was degraded into small organic molecules after the pretreatment, which further acted as the substrate for photoreforming. Mesoporous ZnIn₂S₄ exhibits high H₂ production efficiency, strong redox ability, and long-term photostability. Furthermore, mesoporous ZnIn₂S₄ could overcome the hindrances of dyes and additives of realistic wasted plastic bags and bottles with high decomposition efficiency, providing an efficient and sustainable strategy for the upcycling of wasted plastics.

 Received 6th April 2023
 Accepted 14th April 2023

DOI: 10.1039/d3ra02279j

rsc.li/rsc-advances

Introduction

Global plastic manufacturing reached 368 million metric tons in 2019, and it is expected to rise further in the following years.^{1–3} Plastics generally have a relatively short service period, and most of the used plastics have become waste and accumulate in landfills or in the natural environment.⁴ Due to their strong chemical inertness, the spontaneous degradation process of plastic waste requires up to centuries, which will cause serious global environmental problems.^{5–7} Plastic pollution not only leads to a global environmental issues, but also a waste of precious resources. Most plastics are derived from fossil fuels, and it is estimated that recycling all plastic waste may save 3.5 billion barrels of oil each year.⁸

There have been four main strategies for treating waste plastics, including landfill, incineration, mechanical and chemical recycling.^{9–12} Among which, incineration is widely used to treat plastic waste, generating heat energy within the combustion process, which could be further transformed to other useful energy such as electric energy.¹³ However,

incineration needs massive energy input, high reaction temperature and the products are difficult to be separated. Therefore, developing new strategy to transform waste plastics into valuable products under mild conditions are urgently required.

Photoreforming means H₂ can be generated from organic substrate and water under the sunlight with a photocatalyst.¹⁴ The photogenerated electrons from the photocatalyst can reduce water to yield H₂.¹⁵ H₂ is a valuable product and it has a high demand in the fields of agriculture, pharmacy, chemical industry, and renewable energy. The first example of photoreforming was TiO₂/Pt photocatalyst,¹⁶ which could reform polyvinyl chloride (PVC) to H₂ in water at room temperature. More recently, Reisner and co-workers reported photoreforming of real-world plastics to generate H₂ and fine chemicals by CdS/CdO_x¹⁷ and Ni₂P|CN_x.^{14,18} More and more photocatalyst have been developed and applied in photocatalytic conversion of wasted plastics to value-added products, such as Nb₂O₅,¹⁹ Ag₂O/Fe-MOF,²⁰ MoS₂/Cd_xZn_{1–x}S,²¹ *etc.*^{22–25} However, the existing photocatalysts present some disadvantages, for example, contains toxic Cd element, wide band gap and need noble metal to generate H₂. It is a big challenge to develop a noble-free, non-toxic, and high efficiency photocatalyst for photoreforming of plastics to generated H₂ and other valuable products.

As a visible light-activated layered ternary metal chalcogenide photocatalyst, ZnIn₂S₄ possesses narrow band gap (2.28 eV), no toxic element, and simple preparation method, thus exhibits excellent performance,²⁶ especially in the field of

^aSchool of Chemical Engineering and Technology, Sun Yat-Sen University, Zhuhai, 519082, P.R. China. E-mail: xuecan@mail.sysu.edu.cn

^bFine Chemical Industry Research Institute, School of Chemistry, Sun Yat-Sen University, Guangzhou, 510275, P.R. China. E-mail: jihb@mail.sysu.edu.cn

 † Electronic supplementary information (ESI) available. See DOI: <https://doi.org/10.1039/d3ra02279j>

‡ These authors contributed equally to this work.



photocatalysis, such as pollutant removal, hydrogen evolution, and reduction of CO₂.^{27–31} Herein, we have realized an efficient visible light driven reforming of plastic waste to H₂ and small organic molecules by mesoporous ZnIn₂S₄. The photocatalyst mesoporous ZnIn₂S₄ was prepared through the low temperature hydrothermal method.^{29,32} Beside PET, PLA, and PU, a variety of realistic waste plastic including plastic bags and bottles could be compatible within the transformation. Compared to the reported photocatalyst, mesoporous ZnIn₂S₄ exhibits higher H₂ production efficiency from PLA under simulated sunlight. The noble-free, simply prepared and nontoxic mesoporous ZnIn₂S₄ photocatalyst provides a new strategy for the sustainable upcycling of waste plastics.

Experimental section

Preparation of mesoporous ZnIn₂S₄

In a typical procedure,³² 1.5 mmol of Zn(CH₃COO)₂·2H₂O and 3.0 mmol of InCl₃ were added into 250 mL deionized water (DI) and stirred for 30 min. After that, 8.0 mmol of thioacetamide (TAA) was added to the solution and stirred for another 30 min. The mixed solution was heated to 95 °C and refluxed for 5 h. The resulting precipitation was collected by centrifugation, rinsed with ethanol and DI water for several times, and finally re-dispersed into 100 mL of DI water. The dispersion was ultrasonicated continuously for 30 min. Mesoporous ZnIn₂S₄ was obtained after cryodesiccation (Scheme 1).

Preparation of ZnIn₂S₄

ZnIn₂S₄ was prepared following the previous report²⁹ with a little modified. 50 mL of glycerol was added into 200 mL H₂O (pH = 2.3) and the solution was stirred for 30 min. 2.36 mmol of ZnCl₂, 4.7 mmol of InCl₃ and 9.4 mmol of TAA was added into the above solution. The mixture was stirred for 30 min and maintained at 80 °C for 2 h under continuous stirring. After cooling to room temperature, the product was collected by centrifugation and rinsed with ethanol several times. ZnIn₂S₄ was obtained after drying in a vacuum at 60 °C.

Sample characterization

The crystallographic phase of the prepared sample was determined by powder X-ray diffraction (Smartlab, Rigaku). The morphologies of the prepared sample were observed by a scanning electron microscope (Zeiss, Gemini 500) and a transmission electron microscope (FEI, Tecnai G2 F30). The specific surface areas of the prepared sample were measured by nitrogen sorption at 77 K on a surface area and porosity analyzer (Micromeritics, ASAP2020M) and calculated by the Barrett–

Joyner–Halenda (BJH) method. X-ray photoelectron spectroscopy (XPS) measurement was recorded on a Thermo Fisher Scientific Nexsa spectrometer (Al Kα, 1486.6 eV). The XPS spectrum was calibrated with respect to the binding energy of the adventitious C 1s peak at 284.8 eV. The UV-vis diffuse-reflectance spectrum (UV-vis DRS) was recorded with a UV-vis spectrophotometer (Shimadzu UV-3600) assembled with an optical integrated sphere using BaSO₄ as the reference. Photoluminescence (PL) spectroscopy and time-resolved PL decay spectra were recorded on a spectrophotometer (Edinburgh FLS980). Electrochemical measurements were recorded on an electrochemical workstation (Chen Hua CHI660E) using a three-electrode system with a 0.5 M Na₂SO₄ solution as the electrolyte. A fluorine-doped tin oxide (FTO) conductive glass, the conductive side of which was coated with a thin sample film by the spin coating method, an Ag/AgCl electrode, and a platinum electrode were used as the working electrode, reference electrode, and counter electrode, respectively. Mott–Schottky analyses was measured in the dark using the impedance potential mode. Photocurrent spectral data was recorded under the manual control of ON/OFF with a 300 W xenon lamp as the excitation light source.

Substrate pretreatment

In a typical procedure, the plastic samples were first frozen and crushed. Then, the aqueous KOH (2 M) and plastic power (50 mg mL⁻¹) were added to the vial in sequence, stirring at 40 °C for 24 h. The mixture was used for photoreforming as below.

Photoreforming experiments

Generally, the above solution was transferred to a 50 mL Pyrex glass photoreactor. 7.5 mg of catalyst and 2.5 mL of DI water were then added, and the final conditions were 25 mg mL⁻¹ substrate, 5 mL of 1 M aqueous KOH and 2.5 mg mL⁻¹ catalyst. The atmosphere of the photoreactor was replaced with N₂ using an atmosphere controller (Perfect Light, AC1000). The photoreactor was irradiated by a solar light simulator (CEAULight, 150 mW cm⁻²) equipped with an air mass filter (AM 1.5G). All samples were kept at 25 °C with continuous stirring during irradiation for 12 h. The accumulation of H₂ was analyzed by gas chromatography on an GC7900 equipped with a thermal conductivity detector using N₂ as the carrier gas. The liquid product was centrifuged. The obtained supernatant 0.15 mL was mixed with D₂O (0.3 mL) and maleic acid deuterium oxide solution (0.1 mL, 50 mg mL⁻¹), which was detected by a nuclear magnetic resonance spectroscopy (Bruker AVANCE, ¹H NMR) for qualitative and quantitative analysis.

EPR

EPR spectra were recorded on an EPR spectrometer (JEOL, JES-FA2000). In the trapping of reactive species, a quartz flat cell (Wilmad, WG-810-A) was used to conduct the control experiments by using a free radical trapping agent DMPO.



Scheme 1 Synthesis scheme of mesoporous ZnIn₂S₄.

Results and discussion

Photocatalyst characterization

The scanning electron microscopy (SEM) images show that both mesoporous ZnIn_2S_4 (Fig. 1a) and ZnIn_2S_4 (Fig. 1b) have nano-sheet structure. The morphology of ZnIn_2S_4 is flower-like hierarchical microsphere composed of plenty of nanosheet. Comparing with ZnIn_2S_4 , mesoporous ZnIn_2S_4 possesses bigger pore but less agglomerated phenomena. The transmission electron microscopy (TEM) image reveals that mesoporous ZnIn_2S_4 have lots of pores, which were formed during cryo-desiccation (Fig. 1c). Energy-dispersive spectroscopy (EDS) elemental mapping confirms that Zn (Fig. 1d), In (Fig. 1e) and S (Fig. 1f) are uniformly distributed across the mesoporous ZnIn_2S_4 .

XRD patterns show that the diffraction peaks of mesoporous ZnIn_2S_4 and ZnIn_2S_4 are 21.2° , 27.5° and 47.3° , corresponding to the crystal faces of (006), (102) and (110), respectively (Fig. 2d). These diffraction characteristics can be ascribed to hexagonal ZnIn_2S_4 (JCPDS card no. 04-009-4787). However, they show different preferred crystal faces due to the different preparation methods. XPS analysis shows that Zn 2p peaks of the mesoporous ZnIn_2S_4 and ZnIn_2S_4 appeared at 1045 and 1022.1 eV (Fig. 2a), In 3d peaks at 452.65 and 445.15 eV (Fig. 2b) and S 2p peaks at 161.9 and 163.0 eV (Fig. 2c). It suggests that mesoporous ZnIn_2S_4 and ZnIn_2S_4 have the same valence state.

The N_2 adsorption-desorption isotherms curves (Fig. 3a) show that the curves of ZnIn_2S_4 belong to H4-type hysteresis loops, while the curves of mesoporous ZnIn_2S_4 belong to H3-type hysteresis loops, indicating that mesoporous ZnIn_2S_4 is a mesoporous material with narrow cracks and ZnIn_2S_4 is a slit pore material formed by the accumulation of lamellar particles, which is consistent to the result of SEM images. Besides, pore size distribution plots confirm that the pores of mesoporous ZnIn_2S_4 are bigger than ZnIn_2S_4 (Fig. 3b), which affect the efficiency of photoreforming of plastics.

Photophysical and electrochemical properties of the photocatalysts play an important role in the photocatalytic activity.³³

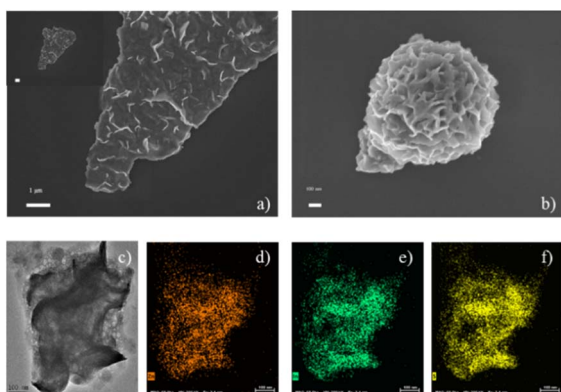


Fig. 1 SEM images of (a) mesoporous ZnIn_2S_4 and (b) ZnIn_2S_4 ; TEM image of (c) mesoporous ZnIn_2S_4 and (d) Zn, (e) In and (f) S atom element mapping of mesoporous ZnIn_2S_4 .

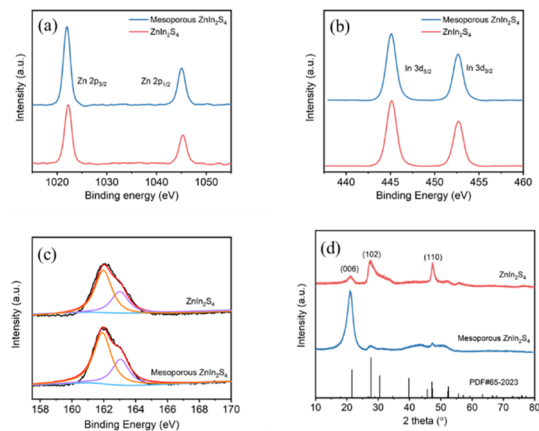


Fig. 2 (a) Zn 2p, (b) In 3d, and (c) S 2p XPS spectra of ZnIn_2S_4 and mesoporous ZnIn_2S_4 . (d) XRD profiles of ZnIn_2S_4 and mesoporous ZnIn_2S_4 .

The UV-vis diffuse-reflectance spectrum (UV-vis DRS) shows that both mesoporous ZnIn_2S_4 and ZnIn_2S_4 can absorb visible light, and the absorption edge of mesoporous ZnIn_2S_4 ($\lambda_{\text{edge}} = 554 \text{ nm}$) is located at longer wavelength than that of ZnIn_2S_4 ($\lambda_{\text{edge}} = 516 \text{ nm}$), which suggest the possibility of high photocatalytic activity of the above materials under visible light (Fig. 4a). To explore the energy band structures of the photocatalyst, Tafel plots and Mott-Schottky plots were performed. According to Tafel plots, the band-gap energy of mesoporous ZnIn_2S_4 and ZnIn_2S_4 were 2.19 eV and 2.32 eV respectively, which indicate that mesoporous ZnIn_2S_4 is more efficient for visible-light utilization than ZnIn_2S_4 (Fig. 4a, inset). Furthermore, Mott-Schottky plots suggest that the two photocatalyst are n-type semiconductors and the flat-band potentials of the mesoporous ZnIn_2S_4 and ZnIn_2S_4 are -0.91 V (vs. Ag/AgCl) and -0.94 V (vs. Ag/AgCl), respectively (Fig. 4b and c). Thus, the valence band (VB) of photocatalyst could be calculated from the band-gap energy (mesoporous ZnIn_2S_4 : 1.28 eV, ZnIn_2S_4 : 1.38 eV). Photocurrent measurements were also conducted to study the ability and stability on the photogenerated charges of mesoporous ZnIn_2S_4 and ZnIn_2S_4 . As shown in Fig. 4d, mesoporous ZnIn_2S_4 is stronger and more stable than ZnIn_2S_4 on the photocurrent response, which indicates the photogenerated charges ability of mesoporous ZnIn_2S_4 is better.

Typically, fluorescence spectroscopy is used to characterize the separation efficiency of photogenerated electron hole

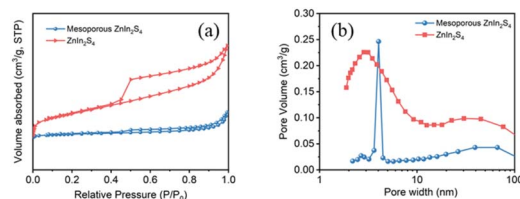


Fig. 3 (a) N_2 adsorption-desorption isotherms and (b) pore size distribution plots of ZnIn_2S_4 and mesoporous ZnIn_2S_4 .

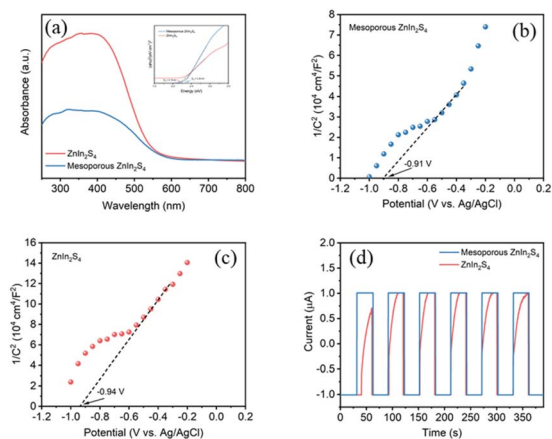


Fig. 4 (a) UV-vis DRS, inset: Tauc plot of samples; Mott–Schottky curves of (b) mesoporous ZnIn_2S_4 and (c) ZnIn_2S_4 ; (d) transient photocurrent response of samples.

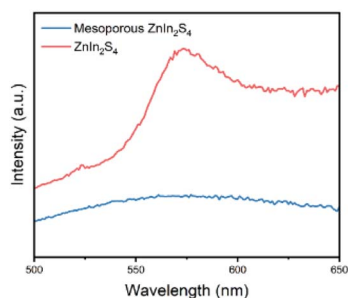


Fig. 5 Stead-state PL spectra of mesoporous ZnIn_2S_4 and ZnIn_2S_4 .

pairs.³⁴ PL spectra of mesoporous ZnIn_2S_4 and ZnIn_2S_4 were recorded at an excitation wavelength of 405 nm (Fig. 5). ZnIn_2S_4 shows a strong fluorescence emission peak at 490 nm, while the fluorescence emission peak of mesoporous ZnIn_2S_4 were nearly quenched, which indicate that the recombination of electrons and holes of mesoporous ZnIn_2S_4 was greatly hindered.

Photoreforming of plastics

The photoreforming performances of as-prepared photocatalysts were evaluated by the hydrogen production of plastics reforming experiments. All conditions, including photocatalyst concentration, substrate concentration and reaction time, were optimized for maximal the H_2 production (Fig. S1†). In a typical procedure, plastics were pretreated in aqueous KOH at 40 °C with continuous stirring for 24 h in the dark. After pretreatment, the photocatalyst was added to the above solution, and the mixture was then transferred to a Pyrex flask, purged with N_2 and irradiated by simulated sun light (AM 1.5G, 150 mW cm^{-2}) at room temperature for certain time.

As for PLA, mesoporous ZnIn_2S_4 exhibits higher hydrogen production efficiency than ZnIn_2S_4 , which was 143.6 $\mu\text{mol g}^{-1} \text{h}^{-1}$ and 70.4 $\mu\text{mol g}^{-1} \text{h}^{-1}$ respectively (Fig. 6a). The different

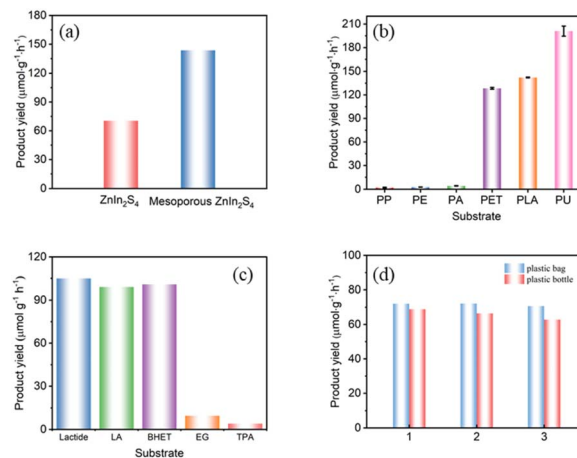


Fig. 6 (a) Photoreforming of PLA with mesoporous ZnIn_2S_4 and ZnIn_2S_4 ; (b) photoreforming of different kinds of plastics; (c) photoreforming performances of dimers and monomers of PET and PLA; and (d) photoreforming performances of commercial plastic bag and bottle with mesoporous ZnIn_2S_4 (1, 2 and 3 are parallel experiment). Reaction conditions: photocatalyst (1.5 mg mL^{-1}), pretreated polymers (25 mg mL^{-1}), aqueous KOH (1 M, 5 mL), and simulated sunlight (AM 1.5 G, 150 mW cm^{-2} , rt), 12 h.

performances of the two photocatalyst might be attributed to the differences of the morphology and pores distribution, and the lamellar structure and mesopores in mesoporous ZnIn_2S_4 make it exhibit better hydrogen production efficiency. Compared with previous reports, the H_2 yield from photoreforming of PLA by mesoporous ZnIn_2S_4 is almost eight times higher than that over CdS/CdO_x and CN_x/NiP (Table 1), while from PET is 3-fold higher than CdS/CdO_x and 14-fold higher than CN_x/NiP , which shows superior H_2 production efficiency.

Mesoporous ZnIn_2S_4 was further employed to a variety of common polymers under simulated sun light. Polypropylene (PP), polyethylene (PE) and polyacrylic acid (PA) could only produce trace amount of hydrogen (H_2), while PET, PLA and polyurethane (PU) performance well, and the order of H_2 production efficiency was $\text{PP} < \text{PE} < \text{PA} < \text{PET} < \text{PLA} < \text{PU}$ under the same reaction conditions (Fig. 6b). As pretreated with aqueous KOH, the ester group of PET, PLA and PU might be

Table 1 Comparison of the photoreforming performance of PLA and PET by different photocatalysts^a

Catalyst	Yield ($\mu\text{mol}_{\text{H}_2} \text{g}_{\text{sub}}^{-1}$)		Reference
	PLA	PET	
Mesoporous ZnIn_2S_4	412.1	472.3	This work
ZnIn_2S_4	356.6	177.7	This work
$\text{CN}_x/\text{Ni}_2\text{P}^b$	59.7 ± 6.0	33.1 ± 1.7	14
CdS/CdO_x^c	54.1 ± 8.9	132 ± 6	17

^a Reaction conditions: pretreated PLA or PET (25 mg mL^{-1}) with all catalyst except $\text{CN}_x/\text{Ni}_2\text{P}$ (which used 50 mg mL^{-1}), KOH or NaOH (aq. 5 mL), catalyst (1.5 mg mL^{-1}), measurements taken after 20 h of simulated sunlight (AM 1.5 G, 100 mW cm^{-2} , rt). ^b $\text{CN}_x/\text{Ni}_2\text{P}$ (1.6 mg mL^{-1}). ^c CdS/CdO_x (1 nmol).

partly decomposed under base environment, and the residue would partial dissolve in the solutions for further photoreforming. It is might be the reason why PET, PLA and PU shows higher H₂ production and degradation efficiency than those of PP, PE and PA.

As for the realistic plastic wastes, which always contain dyes, additives and many kinds of impurities, might make them more difficult to be photocatalytic degradation than the pure one. To evaluate the performance of the real-world plastics over mesoporous ZnIn₂S₄, the photoreforming of plastic bags and plastic bottle were conducted. As shown in Fig. 6d, the H₂ production efficiency from realistic plastic bag and plastic bottle were achieved respective in 72.2 μmol g⁻¹ h⁻¹ and 68.9 μmol g⁻¹ h⁻¹ under the same conditions for the photocatalytic degradation in Fig. 6b. The main component of plastic bags and bottles are PLA and PET, respectively. Comparing the results presented in Fig. 6b with 6d, the additives within the plastic bags and bottles hindered their photoreforming performances significantly.

¹H NMR and ¹³C NMR spectra (Fig. S2†) of the liquid phase product of PLA after photoreforming for 12 h indicate that PLA was decomposed into small organic molecules, such as lactic acid (LA), by mesoporous ZnIn₂S₄ under simulated sun light. Some of LA were further oxidized to pyruvic acid. As shown in Fig. S3,† PET was transferred into ethylene glycol (EG) and terephthalate (TPA) after the pretreatment, and the oxidation product of EG, acetic acid and 2-hydroxyacetic acid were detected in the liquid phase product, showing that mesoporous ZnIn₂S₄ has strong oxidation capacity. The quantitative analysis results showed that the lactic acid in the solution after pretreatment was approximately 28.3 mg, while after photoreforming the amount of LA increased to 61.7 mg with 4.4 mg of pyruvic acid. Combining the result of Fig. S1(b),† it indicated that lactic acid was generated after the pretreatment with KOH, which was further oxidized into valuable small organic molecules by mesoporous ZnIn₂S₄ during the photoreforming. Besides, there is no CO₂ detected during the process.

The monomers and dimers of PLA and PET, including lactic acid (LA), lactide, ethylene glycol (EG), terephthalate (TPA) and bis(2-hydroxyethyl) terephthalate (BHET), were further applied to investigate the photoreforming mechanism over mesoporous ZnIn₂S₄. As shown in Fig. 6c, the H₂ yield from LA (105.0 μmol g⁻¹ h⁻¹) and lactide (99.0 μmol g⁻¹ h⁻¹) were close to that from PLA (142.8 μmol g⁻¹ h⁻¹), which indicate that mesoporous ZnIn₂S₄ could decompose the ester group and further oxidize the monomers derived from PLA to pyruvic acid. As for the monomer and dimer of PET, the H₂ yield from EG (9.6 μmol g⁻¹ h⁻¹) and TPA (4.1 μmol g⁻¹ h⁻¹) was much lower than that from PET (129.7 μmol g⁻¹ h⁻¹), and the H₂ yield from BHET (100.8 μmol g⁻¹ h⁻¹) was close to that from PET. It is might cause that mesoporous ZnIn₂S₄ could decompose the ester group of PET and BHET, but the oxidation ability of mesoporous ZnIn₂S₄ is not enough for EG or TPA. The liquid phase product of monomers and dimers of PLA and PET were analyzed by ¹H NMR and ¹³C NMR as shown in Fig. S4 and S5.†

To evaluate the photostability of mesoporous ZnIn₂S₄ in aqueous KOH, a long-term photoreforming of PLA and PET were conducted. According to the result, the H₂ yield from PLA

kept raising from the first day to the fourth day, it is because more and more PLA were dissolved in the solution and decomposed into oligomers and monomers for further photoreforming. While in the last day, the H₂ production rate went down a little bit which was limited by the total amount of substrate in the solution (Fig. 7a). As for PET, the H₂ yield kept raising from the first day to the end. The total amount of H₂ yield from PET is less than that from PLA after photoreforming for 5 days and the fastest H₂ yield rate from PET is slower than from PLA (Fig. 7b). It is probably because the monomers of PET, EG and TPA, are difficult to be oxidized by mesoporous ZnIn₂S₄, which limits the H₂ yield from PET.

Mechanism investigation

To investigate the mechanism of photoreforming of plastics, electron paramagnetic resonance (EPR) measurement was conducted to test free radicals,³⁵ which were trapped by dimethyl pyrroline oxide (DMPO, radical scavenger). PLA was used as the model substrate, reformed by mesoporous ZnIn₂S₄ under a N₂ atmosphere. Without substrate, hydroxyl radical (·OH) and superoxide radical (·OOH) could be detected when the mixture was irradiated by simulated sun light (Fig. 8a), which suggest that mesoporous ZnIn₂S₄ could generate not only electron-hole pairs, but also free radicals with strong oxidation. When the pretreated PLA solution was added into the above solution, all free radicals disappeared, which suggest that PLA could combine with the free radicals, then the oxidation reactions occurred. As shown in Fig. 8b, when mesoporous ZnIn₂S₄ and ZnIn₂S₄ irradiated by the simulated sun light, there were no significant difference in the EPR spectra.

Combine with the results as shown above and references,^{14,17,32} the mechanism of photoreforming of plastics over mesoporous ZnIn₂S₄ is proposed as following: mesoporous ZnIn₂S₄ could absorb simulated sun light, generating electron-hole pairs and free radicals. Depolymerization and oxidation reaction of PLA would take place with the combined action of hole and free radicals generated from mesoporous ZnIn₂S₄. PLA was decomposed to oligomers and monomer and further oxidized to pyruvic acid. At the meantime, H₂O combined with the electrons on the surface of the photocatalyst could generate pure hydrogen through reduction reaction. Through the above reactions, plastic have been depolymerized into small organic molecules and produce pure H₂.

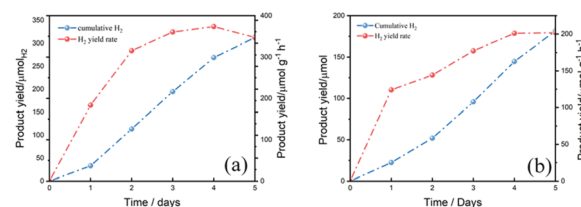


Fig. 7 Long-term photoreforming of (a) PLA and (b) PET. Reaction conditions: photocatalyst (1.5 mg mL⁻¹), pretreated polymers (25 mg mL⁻¹), aqueous KOH (1 M, 5 mL), and simulated sunlight (AM 1.5 G, 150 mW cm⁻², rt).

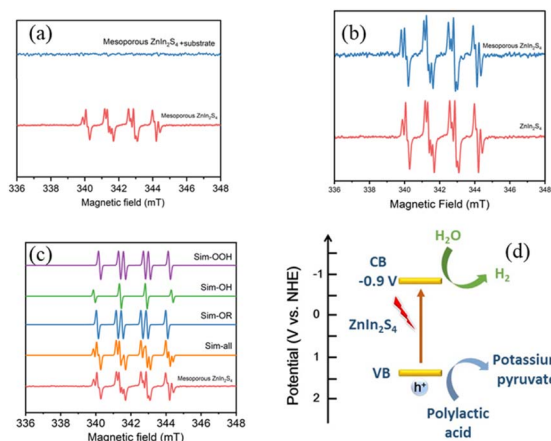


Fig. 8 EPR spectra of free radicals captured by DMPO of (a) mesoporous ZnIn₂S₄ under simulated solar light with or without substrate; (b) mesoporous ZnIn₂S₄ and ZnIn₂S₄ under simulated solar light without substrate (c) simulation of EPR spectra of free radicals captured by DMPO of mesoporous ZnIn₂S₄; (d) proposed mechanism for photoreforming of PLA by mesoporous ZnIn₂S₄.

Conclusions

In this work, we have realized the recycling and utilization of plastic waste through the green and environmental-friendly photoreforming over mesoporous ZnIn₂S₄. PLA, PET and PU were firstly depolymerized into oligomers and monomers with the help of KOH. And driven by the visible light, oligomers could be depolymerized into small organic molecules, which was further oxidized by mesoporous ZnIn₂S₄ at room temperature with hydrogen generated. The strong redox ability, efficient separation of photogenerated electron hole pairs and long-term photostability of the catalyst promoting the reforming of plastics in high efficiency. Albeit hindered by dyes and additives, the plastic bags and bottles could also be reformed efficiently. No carbon dioxide was detected during the photocatalytic process. The noble-free, easy-preparation and non-toxic ZnIn₂S₄ photocatalyst provides an efficient and sustainable strategy for the plastic waste upcycling.

Author contributions

Yeqin Zheng: data curation, software, investigation, visualization, writing – review & editing. Ping Fan: methodology, investigation, writing-original draft, validation, formal analysis. Rongjie Guo: validation. Xiaohui Liu: validation. Xiantai Zhou: resources. Can Xue: conceptualization, resources, validation, writing – review & editing, funding acquisition. Hongbing Ji: resources, review, funding acquisition.

Conflicts of interest

There are no conflicts to declare.

Acknowledgements

This work was financially supported by the National Key Research and Development Program Nanotechnology Specific Project (No. 2020YFA0210900), National Natural Science Foundation of China (No. 21908256, 21938001).

References

- X. Chen, Y. Wang and L. Zhang, *ChemSusChem*, 2021, **14**, 4137–4151.
- H. Li, H. A. Aguirre-Villegas, R. D. Allen, X. Bai, C. H. Benson, G. T. Beckham, S. L. Bradshaw, J. L. Brown, R. C. Brown, V. S. Cecon, J. B. Curley, G. W. Curtzwiler, S. Dong, S. Gaddameedi, J. E. García, I. Hermans, M. S. Kim, J. Ma, L. O. Mark, M. Mavrikakis, O. O. Olafasakin, T. A. Osswald, K. G. Papanikolaou, H. Radhakrishnan, M. A. S. Castillo, K. L. Sánchez-Rivera, K. N. Tumu, R. C. V. Lehn, K. L. Vorst, M. M. Wright, J. Wu, V. M. Zavala, P. Zhou and G. W. Huber, *Green Chem.*, 2022, **24**, 8899–9002.
- R. A. Sheldon and M. Norton, *Green Chem.*, 2020, **22**, 6310–6322.
- R. Geyer, J. R. Jambeck and K. L. Law, *Sci. Adv.*, 2017, **3**, e1700782.
- W. Cornwall, *Science*, 2021, **373**, 36–39.
- M. MacLeod, H. P. H. Arp, M. B. Tekman and A. Jahnke, *Science*, 2021, **373**, 61–65.
- K. L. Law and R. C. Thompson, *Science*, 2014, **345**, 144–145.
- A. Rahimi and J. M. Garcia, *Nat. Rev. Chem.*, 2017, **1**, 0046.
- K. Ragaert, L. Delva and K. Van Geem, *Waste Manage.*, 2017, **69**, 24–58.
- J. M. Garcia and M. L. Robertson, *Science*, 2017, **358**, 870–872.
- S. Ügdüler, K. M. V. Geem, R. Denolf, M. Roosen, N. Mys, K. Ragaert and S. D. Meester, *Green Chem.*, 2020, **22**, 5376–5394.
- D. D. Pham and J. Cho, *Green Chem.*, 2021, **23**, 511–525.
- D. P. Serrano, J. Aguado and J. M. Escola, *ACS Catal.*, 2012, **2**, 1924–1941.
- T. Uekert, H. Kasap and E. Reisner, *J. Am. Chem. Soc.*, 2019, **141**, 15201–15210.
- S. Chu, B. Zhang, X. Zhao, H. S. Soo, F. Wang, R. Xiao and H. Zhang, *Adv. Energy Mater.*, 2022, **12**, 2200435.
- T. Kawai and T. Sakata, *Chem. Lett.*, 1981, **10**, 81–84.
- T. Uekert, M. F. Kuehnel, D. W. Wakerley and E. Reisner, *Energy Environ. Sci.*, 2018, **11**, 2853–2857.
- T. Uekert, M. A. Bajada, T. Schubert, C. M. Pichler and E. Reisner, *ChemSusChem*, 2021, **14**, 4190–4197.
- X. Jiao, K. Zheng, Q. Chen, X. Li, Y. Li, W. Shao, J. Xu, J. Zhu, Y. Pan, Y. Sun and Y. Xie, *Angew. Chem., Int. Ed.*, 2020, **59**, 15497–15501.
- J. Qin, Y. Dou, F. Wu, Y. Yao, H. R. Andersen, C. Hélix-Nielsen, S. Y. Lim and W. Zhang, *Appl. Catal., B*, 2022, **319**, 121940.
- Y. Li, S. Wan, C. Lin, Y. Gao, Y. Lu, L. Wang and K. Zhang, *Sol. RRL*, 2021, **5**, 2000427.

- 22 I. Nabi, A.-U.-R. Bacha, K. Li, H. Cheng, T. Wang, Y. Liu, S. Ajmal, Y. Yang, Y. Feng and L. Zhang, *iScience*, 2020, **23**, 101326.
- 23 B. Cao, S. Wan, Y. Wang, H. Guo, M. Ou and Q. Zhong, *J. Colloid Interface Sci.*, 2022, **605**, 311–319.
- 24 M. Han, S. Zhu, C. Xia and B. Yang, *Appl. Catal., B*, 2022, **316**, 121662.
- 25 C. Xing, G. Yu, J. Zhou, Q. Liu, T. Chen, H. Liu and X. Li, *Appl. Catal., B*, 2022, **315**, 121496.
- 26 J. Wang, S. Sun, R. Zhou, Y. Li, Z. He, H. Ding, D. Chen and W. Ao, *J. Mater. Sci. Technol.*, 2021, **78**, 1–19.
- 27 D. Yuan, M. Sun, S. Tang, Y. Zhang, Z. Wang, J. Qi, Y. Rao and Q. Zhang, *Chin. Chem. Lett.*, 2020, **31**, 547–550.
- 28 J. Qiu, M. Li, L. Yang and J. Yao, *Chem. Eng. J.*, 2019, **375**, 121990.
- 29 C. Jiang, H. Wang, Y. Wang and H. Ji, *Appl. Catal., B*, 2020, **277**, 119235.
- 30 R. M. Mohamed, A. Shawky and M. S. Aljahdali, *J. Taiwan Inst. Chem. Eng.*, 2016, **65**, 498–504.
- 31 C. Chen, W. Hou and Y. Xu, *Appl. Catal., B*, 2022, **316**, 121676.
- 32 L. Huang, B. Han, X. Huang, S. Liang, Z. Deng, W. Chen, M. Peng and H. Deng, *J. Alloys Compd.*, 2019, **798**, 553–559.
- 33 L. Zhang, J. Ran, S.-Z. Qiao and M. Jaroniec, *Chem. Soc. Rev.*, 2019, **48**, 5184–5206.
- 34 S. Zhang, H. Gao, X. Liu, Y. Huang, X. Xu, N. S. Alharbi, T. Hayat and J. Li, *ACS Appl. Mater. Interfaces*, 2016, **8**, 35138–35149.
- 35 Z. Wang, W. Ma, C. Chen, H. Ji and J. Zhao, *Chem. Eng. J.*, 2011, **170**, 353–362.